REVIEWS

Journal of Semiconductors
(2024) 45, 021801
doi: 10.1088/1674-4926/45/2/021801

Research progress of alkaline earth metal iron-based oxides as anodes for lithium-ion batteries

Mingyuan Ye[1, ‡], Xiaorui Hao[2, ‡], Jinfeng Zeng[3], Lin Li[4, †], Pengfei Wang[1], Chenglin Zhang[5, †], Li Liu[1], Fanian Shi[1, †], and Yuhan Wu[1, 6, †]

[1]School of Environmental and Chemical Engineering, Shenyang University of Technology, Shenyang 110870, China

[2]College of Materials Science and Engineering, Nanjing Tech University, Nanjing 211816, China

[3]College of Pharmacy, Xinjiang Medical University, Engineering Research Center of Xinjiang and Central Asian Medicine Resources (Ministry of Education), Urumqi 830000, China

[4]Institute for Carbon Neutralization, College of Chemistry and Materials Engineering, Wenzhou University, Wenzhou 325035, China

[5]School of Physics and Electronic Engineering, Jiangsu University, Zhenjiang 212013, China

[6]Key Laboratory of Advanced Energy Materials Chemistry (Ministry of Education), Nankai University, Tianjin 300071, China

Abstract: Anode materials are an essential part of lithium-ion batteries (LIBs), which determine the performance and safety of LIBs. Currently, graphite, as the anode material of commercial LIBs, is limited by its low theoretical capacity of 372 mA·h·g^{-1}, thus hindering further development toward high-capacity and large-scale applications. Alkaline earth metal iron-based oxides are considered a promising candidate to replace graphite because of their low preparation cost, good thermal stability, superior stability, and high electrochemical performance. Nonetheless, many issues and challenges remain to be addressed. Herein, we systematically summarize the research progress of alkaline earth metal iron-based oxides as LIB anodes. Meanwhile, the material and structural properties, synthesis methods, electrochemical reaction mechanisms, and improvement strategies are introduced. Finally, existing challenges and future research directions are discussed to accelerate their practical application in commercial LIBs.

Key words: alkali-earth metal iron-based oxides; anodes; lithium-ion batteries; electrochemical energy storage

Citation: M Y Ye, X R Hao, J F Zeng, L Li, P F Wang, C L Zhang, L Liu, F N Shi, and Y H Wu, Research progress of alkaline earth metal iron-based oxides as anodes for lithium-ion batteries[J]. *J. Semicond.*, 2024, 45(2), 021801. https://doi.org/10.1088/1674-4926/45/2/021801

1. Introduction

Energy storage technologies have received extensive attention in recent decades, in which metal ion batteries are one of the promising candidates[1–6]. Among various emerging metal ion batteries, lithium-ion batteries (LIBs) are the most successful and widely used in electric vehicles and portable electronic devices because of their high operating voltage, low self-discharge effect, long cycle life, high energy density, and superior safety[7–9]. An ideal anode material should have suitable lithium insertion potential, high theoretical specific capacity, good electronic conductivity, and superior structural stability. Meanwhile, it should meet the requirement of low cost and environmental friendliness[10, 11]. Conventional graphite anodes have a stable voltage plateau during discharging and charging, and have been widely applied in commercial LIBs. However, its theoretical specific capacity is only 372 mA·h·g^{-1}, which considerably limits the large-scale application of LIBs. In this case, developing anode materials with high electrochemical performance is of great necessity to replace graphite.

Since Poizot *et al*.[12] first reported transition metal oxides as anode materials of LIBs, transition metal oxide-based anodes have attracted wide attention, among which iron oxides show great potential because of their high theoretical capacity, abundant raw material, low cost, and environmental benignity[13, 14]. During lithiation processes, iron ions (Fe^{3+} and Fe^{2+}) are converted into metallic iron (Fe^0), thus delivering a high capacity (924–1007 mA·h·g^{-1})[15, 16]. The iron oxide family includes many members with different crystal structures, morphologies, and valence states. They all exhibit good lithium storage capability as LIB anodes. Nonetheless, the electrochemical performance, such as cycling stability and rate capability, still needs improvement. The main reason is the significant volume change during lithium insertion/extraction, resulting in material pulverization and delamination[17–19]. Introducing another metallic element to construct iron-based binary metal oxides is a promising way to offset these issues. First, different metal elements have different expansion coefficients. The synergistic effect between them can alleviate volume changes[20]. Second, adding highly electrochemically active metal elements can dramatically improve lithium storage capability[21]. Third, multi-metal elements reduce the electron transition barrier, enhancing intrin-

Mingyuan Ye and Xiaorui Hao contributed equally to this work and should be considered as co-first authors.

Correspondence to: L Li, linli@wzu.edu.cn; C L Zhang, chenglinzhang@ujs.edu.cn; F N Shi, shifn@sut.edu.cn; Y H Wu, yuhanwu@sut.edu.cn

Received 20 SEPTEMBER 2023; Revised 18 OCTOBER 2023.

Table 1. Comparing the physical, chemical, and economic parameters of alkaline earth metal elements.

	Mg	Ca	Sr	Ba
Atomic number	12	20	38	56
Atomic mass (g·mol^{-1})	24.305	40.078	87.62	137.327
Abundance in earth's crust (%)	2.33	4.15	0.037	0.0425
Melting point (°C)	651	842	769	725
Ionic radius (Å)	0.72	1	1.18	1.35
Distribution	22.5% in China	Everywhere	37.9% in Spain	29% in China
Price of nitrate (US $ per kg)	2.23	2.21	6.53	0.246

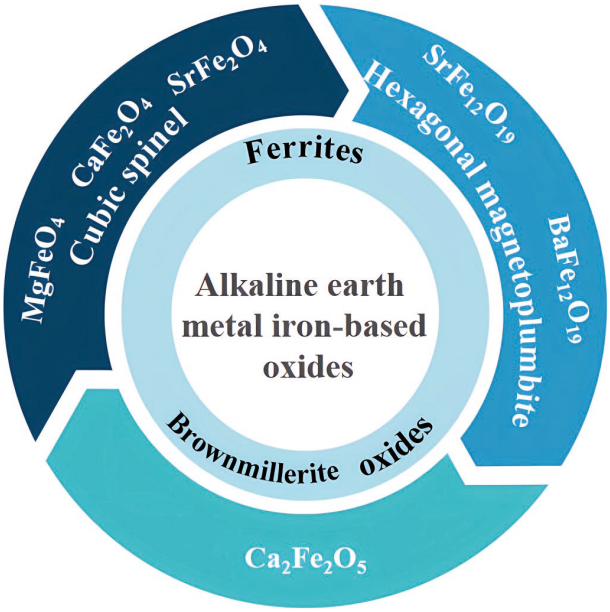

Fig. 1. (Color online) The classification of alkaline earth metal iron oxides and their representative materials as anodes for LIBs.

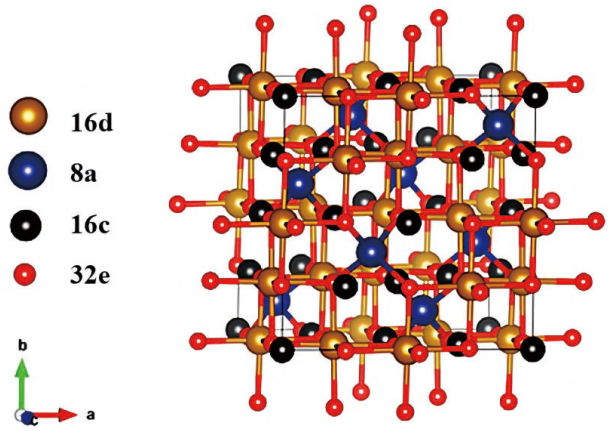

Fig. 2. (Color online) Representative structure of spinel ferrite oxides viewed down the (001) axis. Cations occupy tetrahedral (8a) sites and octahedral (16d) sites, with oxygen atoms at the 32e sites. Octahedral (16c) vacancies in the structure are also indicated[30]. (Reprinted with permission, Copyright 2020, The Royal Society of Chemistry).

sic electronic conductivity[22]. Fourth, the structure, composition, and morphology, which play a crucial role in material properties and electrochemical performance, are highly changeable[23, 24].

Alkaline earth metals (Mg, Ca, Sr, Ba) as additives exhibit significant advantages, such as high elemental abundance, low raw price, and superior environmental friendliness (Table 1). During electrochemical reaction processes, some materials generate MgO, CaO, and other non-active components, which can alleviate the problems of volume change and electrode pulverization caused by high working potential, thereby prolonging the cycling life[25, 26]. Given these points, this work summarizes the classification (Fig. 1) and research progress of the reported alkaline earth metal iron-based oxide LIB anodes. Meanwhile, material and structural properties, synthesis methods, electrochemical reaction mechanisms, and improvement strategies are introduced. According to the current development, existing challenges and future research directions are proposed. We hope this review can provide comprehensive information on alkaline earth metal iron-based oxides to promote their further development and practical applications.

2. Alkaline earth metal ferrites

Alkaline earth metal ferrites are a widely used magnetic material. They have the characteristics of high permeability, high resistivity, low price, and easy preparation[27, 28]. According to the crystal structure, ferrites can be divided into cubic spinel, rare-earth garnet, and hexagonal magnetoplumbite[29]. Among them, cubic spinel ferrites are composed of divalent metal ions with a similar ionic radius to Fe^{2+} or multiple metal ion groups with an average chemical valence of divalent. The chemical formula is MFe_2O_4 (M = divalent metal ions, such as Zn, Co, and Ni), where Fe^{3+} can be replaced by other trivalent metal ions (e.g., Al^{3+} and Cr^{3+}). The chemical formula of rare-earth-iron garnets is $R_3Fe_5O_{12}$, where R denotes trivalent rare earth metal ions, such as Ln^{3+}, Y^{3+}, Sm^{3+}, and Gd^{3+}. Hexagonal magnetoplumbite ferrites have six different structures, and the chemical formula of binary iron-based metal oxides is $MeFe_{12}O_{19}$, where Me = Ba, Sr, Pb, etc.

According to cation occupancy, cubic spinel MFe_2O_4 (Fig. 2) can be divided into normal, inverse, and mixed. In normal spinel, the oxygen-ions pack tightly, the trivalent cations occupy the octahedral space of the six-coordinated, and the divalent cations occupy the tetrahedral space of the four-coordinated, including $MgAl_2O_4$, $ZnFe_2O_4$, $CdFe_2O_4$, etc. In inverse spinel, such as $CoFe_2O_4$ and $NiFe_2O_4$, divalent cations and half-trivalent cations occupy the octahedral voids. The other half of trivalent cations occupy the tetrahedral space, expressing as $[B^{3+}][A^{2+}B^{3+}]O_4$. In mixed spinel, A and B cations occupy the octahedral and tetrahedral positions, and the molecular formula is $[M^{2+}_xFe^{3+}_{1-x}][M^{2+}_{1-x}Fe^{3+}_{1+x}]O_4$, including $NiCo_2O_4$, $MnCo_2O_4$, and $CoMn_2O_4$. The cubic spinel MFe_2O_4 is obtained by pairing iron ions with suitable divalent metal cations which occupy tetrahedral or octahedral positions. This system can take full advantage of multi-component and overcome the disadvantages of metal oxides, such as substan-

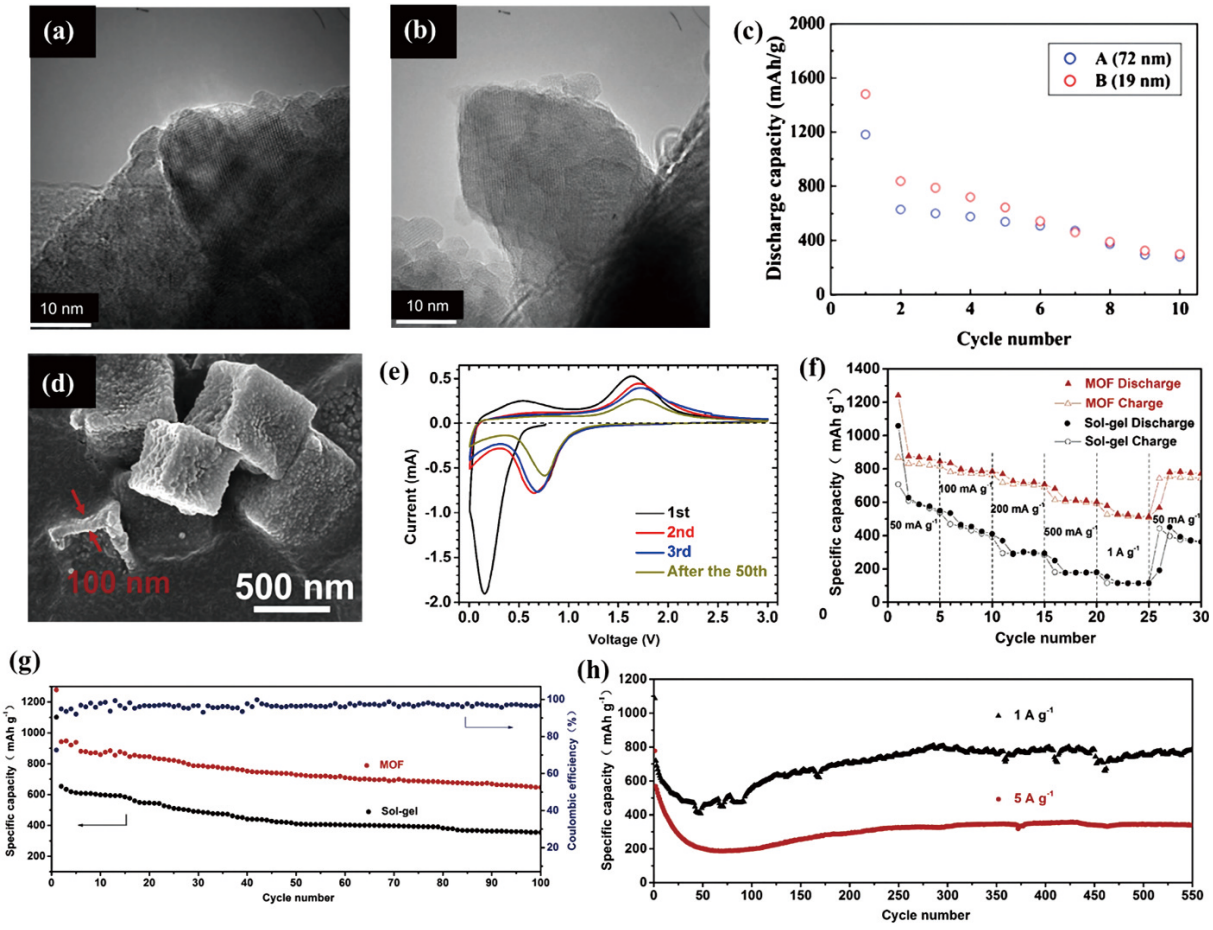

Fig. 3. (Color online) Transmission electron microscope (TEM) images of $MgFe_2O_4$ spinel: (a) as-prepared and (b) 15 h milled. (c) Cyclic performance of $MgFe_2O_4$ spinel samples: (A) as-prepared and (B) 15 h milled sample[36] (Reprinted with permission, Copyright 2011, Elsevier). (d) SEM images of $MgFe_2O_4$ microboxes. (e) Cyclic voltammetry curves of the MOF $MgFe_2O_4$ sample at a scan rate of 0.1 $mV{\cdot}s^{-1}$. (f) Rate performance of the $MgFe_2O_4$ derived from MOF and sol-gel methods at current densities from 0.05 to 1.0 $A{\cdot}g^{-1}$. (g) Charge/discharge curves of the $MgFe_2O_4$ derived from MOF and sol-gel methods at a current density of 50 $mA{\cdot}g^{-1}$. (h) Cyclic performance of MOF $MgFe_2O_4$ for the first 550 cycles at a current density of 1.0 and 5.0 $A{\cdot}g^{-1}$[45] (Reprinted with permission, Copyright 2017, Elsevier).

tial initial discharge capacity loss and poor cycling stability. Alkaline earth metal cubic spinel ferrites $MeFe_2O_4$ (Me = Mg, Ca, Sr, and Ba) as anodes for LIBs can provide more lithium insertion sites, thus delivering higher theoretical specific capacities about three times higher than carbon materials.

Spinel ferrites are one of the most promising electrode materials for energy storage because of their distinct discharge and charging plateaus, high theoretical specific capacities, and high electrical conductivity[31]. The composition and microstructure of nano ferrites significantly affect properties and are tightly related to preparation methods and conditions. Currently, many researchers focus on developing simple and effective synthesis methods to control grain size and morphology to realize the regulation of the material properties[32–35]. In 2011, Sivakumar *et al.*[36] studied the application of $MgFe_2O_4$ as an anode (Figs. 3(a)–3(c)). $MgFe_2O_4$ nanoparticles were successfully prepared by a ball milling method with an initial discharge capacity of 1480 $mA{\cdot}h{\cdot}g^{-1}$, but the capacity rapidly decayed in the following cycles (only 300 $mA{\cdot}h{\cdot}g^{-1}$ after ten cycles). The typical preparation strategies of ferrites include co-precipitation, sol-gel, hydrothermal, and molten salt methods[37–44]. Among them, the hydrothermal method is a popular option to synthesize nanosized ferrites and has been widely adopted. For example, Prussian blue (PB) $[Fe_4(Fe(CN)_6)_3]$ microcubes were synthesized by a hydrothermal method and used as self-sacrificing templates to prepare uniform $MgFe_2O_4$ microboxes (Figs. 3(d) and 3(e))[45]. The $MgFe_2O_4$ microbox shell consisted of microcrystals with an average size of about 24 nm. Compared with solid $MgFe_2O_4$ synthesized by a conventional sol-gel method, PB-derived $MgFe_2O_4$ exhibited better cycle and rate performance (Figs. 3(f) and 3(g)). The initial discharge capacity was as high as 1278 $mA{\cdot}h{\cdot}g^{-1}$. Furthermore, when the current density was 1 $A{\cdot}g^{-1}$ after 550 cycles, the specific capacity reached 781 $mA{\cdot}h{\cdot}g^{-1}$ (Fig. 3(h)). The first reason for the superior performance was that the PB-derived $MgFe_2O_4$ had a unique cubic hollow structure with a porous shell, which provided high surface areas between electrodes and electrolytes, facilitating charge transfer and Li^+ diffusion[46]. The second reason was that the $MgFe_2O_4$ was decomposed into MgO, which buffered the fragmentation and aggregation of Fe and Fe_2O_3 during the cycle. Adding elements, such as Ca, Mg, or Sr, as cushioning substances into the metal oxides improved the electrochemical performance effectively.

It is possible to investigate the reaction mechanism of alkaline earth metal iron-based oxide anodes by progressively exploring the reaction mechanism of metal oxides. Generally, the reaction mechanism of metal oxide anodes is a conver-

sion reaction. The reversible electrochemical reaction of Li^+ with transition metal oxides M_xO_y (M = Co, Ni, Cu, or Fe) is similar to the redox reaction (Eq. (1)):

$$M_xO_y + 2yLi^+ + 2ye^- \leftrightarrow xM + yLi_2O. \quad (1)$$

The formation of a new phase may lead to significant volume change and capacity decay. In the later cycles, the capacity loss may be due to the solid electrolyte interface (SEI) irreversibly consuming Li^+, reducing Li^+ insertion and detachment reversibility. For non-oxides (TM_xQ_y, TM = transition metal, Q = S or Se), the reversible electrochemical transformation reaction can be expressed as (Eq. (2)).

$$TM_xQ_y + 2yLi^+ + 2ye^- \leftrightarrow xTM + yLi_2Q. \quad (2)$$

Each TM_xQ_y can combine $2y$ Li^+ to form TM and Li_2Q in nanoparticles with a specific capacity of more than 500 mA·h·g^{-1}.

To investigate whether there is a general reaction mechanism in alkaline earth metal cubic spinel ferrites, Permien *et al*.[47] analyzed the redox mechanism of $MgFe_2O_4$ with different sizes by using X-ray diffraction (XRD), ^{7}Li nuclear magnetic resonance spectroscopy and ^{57}Fe Mössbauer spectroscopy. The results showed that the lithiation mechanism depended on the average size of the particles. At the beginning of the reaction, a small amount of Li^+ was embedded in tiny $MgFe_2O_4$ particles. In contrast, large $MgFe_2O_4$ particles did not undergo such a reaction. When embedded in $2Li^+$, all Fe^{3+} were reduced to Fe^{2+}. All magnesium and iron ions moved from tetrahedral to octahedral vacancies, transforming into disordered NaCl-type. After inserting $4Li^+$, Fe^{2+} was wholly reduced to metallic Fe. To further explore the lithium insertion/extraction mechanisms, three spinel ferrites (Fe_3O_4, $MgFe_2O_4$, and $ZnFe_2O_4$) with inverse, normal, and partially inverse were prepared[30]. During the initial discharge, the lithiation of the three spinel ferrites was carried out by partially occupying the $[A]_{16c}[B_2]_{16d}O_4$ phase at the 16c site, and the cations rearranged in the framework. In the Li^+ extraction process, iron ions were in a coordination structure with low inversion symmetry. By analyzing the local atomic structure of extended X-ray absorption fine structure (EXAFS) data, $MgFe_2O_4$ and $ZnFe_2O_4$ containing +2 valence cations exhibited a separation of the FeO from the MgO or ZnO phase during the charge state, indicating that the substitution of +2 valent cations showed a significant effect on the properties of the delithiated phase in the material. In addition to the above research on the reaction mechanism of spinel ferrites, the contribution of different surfaces of $MgFe_2O_4$ with three spinel structures (normal-, mixed-, and inverse-) to the discharge performance was explored by density functional theory (DFT)[48]. In the initial state, Li^+ accumulated on each surface and were transported downward. The $MgFeO_x$-terminated mixed-spinel (100) surface was the most active among various stable surfaces. It provided superior capacities, high voltages, and convenient lithium-ion transport. Such a high performance correlated with functional surfaces that could trap and accommodate large amounts of Li^+ and promote continuous smooth transportation to the subsurface.

Although alkaline earth metal cubic spinel ferrites anodes display a high specific capacity, they still suffer problems of iron-based oxides, such as poor conductivity, easy fragmentation, inferior cycling stability, and undesirable initial coulombic efficiency (ICE). Therefore, solving these problems by modification has become one of the essential hotspots. Among various modification methods, constructing carbon composite structures is a standard promising way[49, 50]. In general, carbon materials have good toughness and flexibility[51–55]. Commonly used carbon-based active materials include carbon nanotubes (CNT)[56, 57], graphene oxides (GO)[58, 59], amorphous carbons, etc[33, 60]. The spherical vesicle $MgFe_2O_4$/G composites were synthesized by a solvothermal method (Fig. 4(a))[61]. Cross-linked graphene layers formed a 3D conductive network, and the $MgFe_2O_4$ nanoparticles were randomly immobilized on the two sides of the self-filled graphene sheets utilizing electrostatic interaction. When a current density was 500 mA·g^{-1}, the initial discharge and charge capacities were 1246 and 896 mA·h·g^{-1}, respectively. The capacity loss was due to the formation of SEI and the irreversible consumption of Li^+ (Fig. 4(b)). After 100 cycles, the specific capacity consistently increased to 1341 mA·h·g^{-1} with a Coulombic efficiency above 98%, which was higher than the theoretical capacity. It was mainly due to the capacitance contribution formed in the interfacial lithium storage and the reversibility of the polymer/gel film. The 3D vesicular $MgFe_2O_4$ on graphene nanosheets delivered excellent electrochemical properties. Firstly, graphene limited the growth of $MgFe_2O_4$ particles to form smaller nanoparticles with more active sites, shortening pathways for Li^+ diffusion. Secondly, the $MgFe_2O_4$/G composites exhibited a higher specific surface area, providing more interfaces for electrolyte penetration. Thirdly, graphene as a 3D conducting network enormously improved electron transport. Also, graphene acted as a substrate that buffered volume expansion, prevented crystal aggregation, and maintained electrode integrity. In addition to the solvothermal method, carbon-coated $MgFe_2O_4$ composites were synthesized by a dual strategy of decomposition and metal thermal reduction[62]. The dual synthesis route prepared ideal core-shell bimetallic oxide composites and helped alleviate the impact of forming unpredictable components. The unique core-shell $MgFe_2O_4$/C nano-composites displayed excellent lithium storage and long-term cycling performance as anodes and offered a capacity of 1150 mA·h·g^{-1} at 100 mA·g^{-1} (Fig. 4(c)). The multiple active centers between carbon layers and $MgFe_2O_4$ particles improved electrochemical reaction kinetics. The reticulated carbon constructed a fast channel for high-speed current output. The micro-framework consisting of carbon layers and particles as a buffer matrix prevented the aggregation of $MgFe_2O_4$ nanoparticles[63]. Furthermore, the $MgFe_2O_4$ crystal structure played a crucial role in the stability of the framework (Fig. 4(d)). Based on this unique structure, the composites showed ultra-high activities and efficient synergistic lithium storage. In the process of Li^+ insertion, Fe^{3+} was converted into Fe^0, and two new phases, MgO and Li_2O, were obtained simultaneously. The unreacted MgO was used as a framework to prevent the accumulation of active particles and accommodate volume changes. With the in-depth study of nano-ferrite anodes, space limitations have gradually attracted wide attention. For example, the sesame straw-like $MgFe_2O_4$/N-doped hollow porous carbon nanofibers (MFO/NPCNF) were synthesized as

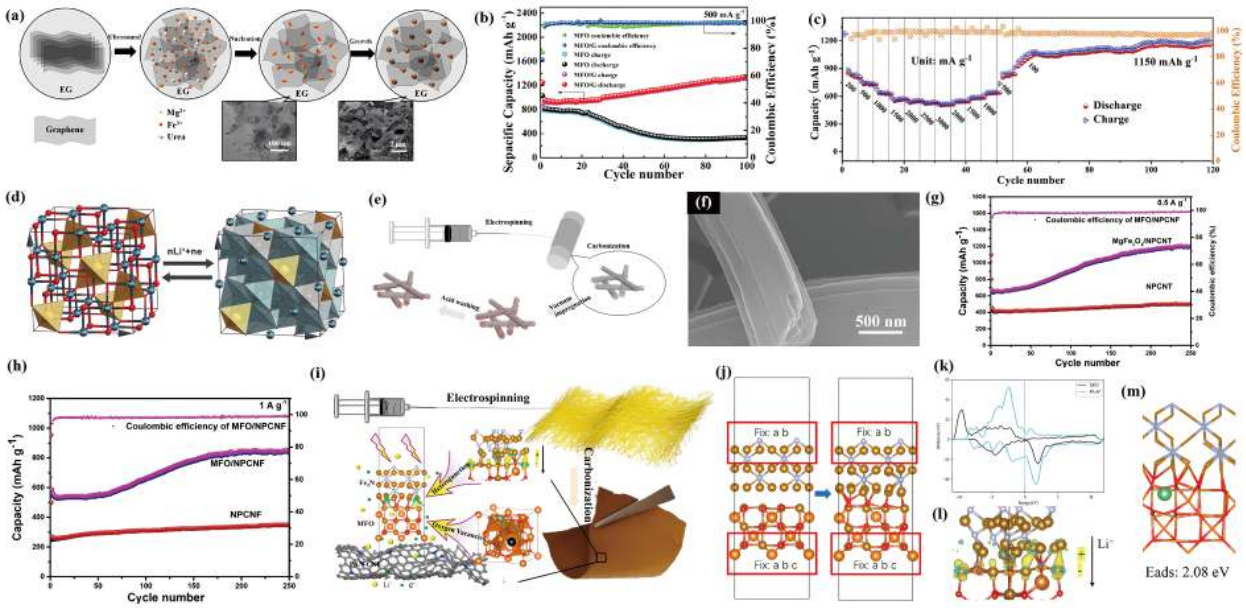

Fig. 4. (Color online) (a) Schematic representation of the synthetic process of $MgFe_2O_4$/G. (b) The cycle performance of $MgFe_2O_4$/G and $MgFe_2O_4$ at 500 mA·g^{-1}[61] (Reprinted with permission, Copyright 2017, The American Chemical Society). (c) $MgFe_2O_4$/C rate capacity and Coulombic efficiency at 200–3000 mA·g^{-1}. (d) Schematic representation of the lithium insertion/de-insertion in the $MgFe_2O_4$ structure[62] (Reprinted with permission, Copyright 2020, Elsevier). (e) Synthetic plot and (f) FESEM plot of the MFO/NPCNF. The cycle performance of NPCNF and MFO/NPCNF at (g) 0.5 A·g^{-1} and (h) 1 A·g^{-1}[64] (Reprinted with permission, Copyright 2021, Elsevier). (i) Schematic diagram of the structure design for the PAN-$MgFe_2O_4$ flexible free-standing anode. (j) Modeling and optimized structure of $MgFe_2O_4$/Fe_3N heterojunction. (k) Electronic density of states of $MgFe_2O_4$/Fe_3N heterojunction. (l) $MgFe_2O_4$/Fe_3N heterojunction differential charge density (isosurface level: 0.015). (m) Adsorption structure of lithium-ions at the $MgFe_2O_4$/Fe_3N heterogeneous interface[72] (Reprinted with permission, Copyright 2022, The American Chemical Society).

anodes using an electrospinning method and a spatial confinement strategy (Figs. 4(e) and 4(f))[64]. The MFO/NPCNF anodes were cycled for 250 cycles at a current density of 500 mA·g^{-1} and 1 A·g^{-1} to obtain a capacity of 1205.8 mA·h·g^{-1} (Fig. 4(g)) and 846.9 mA·h·g^{-1} (Fig. 4(h)), respectively. Its excellent cycling and rate performance was due to the following points[65, 66]: (1) one-dimensional NPCNF had hollow porous channels that provided directed electron/ion conducting pathways to facilitate electrolyte penetration and mitigate volume expansion; (2) *in situ* growth and uniformly dispersed of ~15 nm spherical MFO nanoparticles in the NPCNF accelerated reaction kinetics; (3) N-doping sites in CNFs interacted with Fe^{3+} to form Fe–N bonds, which could enhance the connection between MFO nanoparticles and CNFs, thereby preventing the aggregation of MFO and improving kinetic performance. In summary, doping increases performance dramatically as a cost-effective and straightforward strategy. Heteroatomic (N, S, F, and P) doping modulates electronic and physicochemical properties. The synergistic effect caused by doping can improve the conductivity of the electrode and promote the reaction between electrodes and lithium-ions[67–71]. Doping may also generate more defects and sites, thereby providing more lithium storage sites, enhancing the diffusion of Li^+, and effectively optimizing electrochemical performance. Co-doping reports have gradually increased in energy storage and have been proven to improve the electrochemical performance of several electrode materials. In addition, it is also possible to add polyacrylonitrile (PAN) to construct a buffer framework for optimizing the electrode performance. For instance, $MgFe_2O_4$ nanoparticles were synthesized by a solvothermal method, and then the prepared $MgFe_2O_4$ nanoparticles were used to obtain PAN-$MgFe_2O_4$ nanofibers by an electrospinning method[72]. During carbonization, the nanoparticles interacted with pyridine N in the PAN layer, and the Fe_3N coating was formed on the surface. The *in situ* formed $MgFe_2O_4$/Fe_3N heterostructure (as shown in Figs. 4(i)–4(m)) established an internal electric field that facilitated Li^+/charge transfer, enhancing the Li^+ adsorption energy and interfacial lithium storage effect. Carbon nanofibers as a skeleton structure provided fast conductive channels, relieving volume expansion and ameliorating cycling stabilities. The abundant oxygen vacancies in $MgFe_2O_4$ changed the electronic structure, increasing the intrinsic conductivity, reducing the Li^+ diffusion energy, weakening the Fe–O bond, and promoting the conversion reaction. Other reports on the cycling performance of alkaline earth metal MFe_2O_4-based electrodes are shown in Table 2, and the table reveals that morphological structures and preparation methods of electrodes significantly affect lithium storage performance. Therefore, to cope with the intense mechanical stress of continuous expansion/contraction in active particles during the lithium insertion/de-insertion process, modulating its morphology and size is vital for developing anodes with excellent capacities and long-cycle stability.

Besides $MgFe_2O_4$, $CaFe_2O_4$ is also naturally abundant, environmentally friendly, and low-cost. Compared to Fe_2O_3, the volume expansion of $CaFe_2O_4$ is not prominent during the cycle. The theoretical capacity of $CaFe_2O_4$ (770 mA·h·g^{-1}) is approximately twice than that of commercial graphite. Furthermore, the density of $CaFe_2O_4$ is much higher than graphite. Therefore, $CaFe_2O_4$ has a higher volume capacity. Solution combustion synthesis (SCS) is a fast and one-step method for preparing metal oxides with high porosity and good uniformity[82, 83]. The porous $CaFe_2O_4$ was prepared by this method

Table 2. Comparison of the cycling performance of alkaline earth metal MFe_2O_4-based electrodes.

Materials (morphological structure)	Synthesis methods	Reversible capacity ($mA{\cdot}h{\cdot}g^{-1}$)/Cycle times	Current density ($mA{\cdot}g^{-1}$)	Refs
$MgFe_2O_4$ nanomicrospheres	Solvothermal method	634/350th	500	[73]
Submicron hollow spherical $MgFe_2O_4$	Solvothermal method	900/70th	107.2	[74]
Porous $CaFe_2O_4$	Sol-gel method	816/100th	100	[75]
Carbon-coated $MgFe_2O_4$	Coprecipitation method	744/160th	100	[76]
Nitrogen-doped carbon-coated $MgFe_2O_4$ nanofibers	Electrospinning method	926/200th	100	[77]
Coralline Fe_2O_3@$MgFe_2O_4$	Gel-cast method	1700/500th	100	[78]
Double-shelled hybrid $MgFe_2O_4$@Fe_2O_3 hollow microspheres	Hydrothermal method	1390/160th	500	[79]
3D porous $MgFe_2O_4$	Hydrothermal method	780/1000th	5000	[80]
$MgFe_2O_4$@$ZnFe_2O_4$@MgO irregular nanosheets	Thermal decomposition and selective etching	500/330th	100	[81]

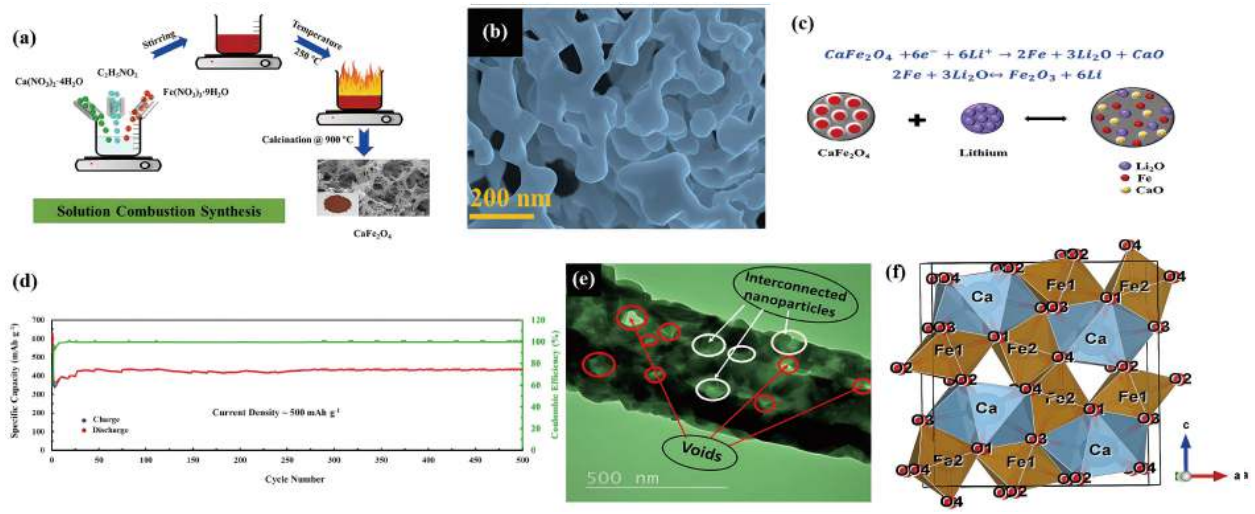

Fig. 5. (Color online) (a) Schematic illustration of the synthesis of $CaFe_2O_4$ via solution combustion technique. (b) HR-FESEM images of as-synthesized $CaFe_2O_4$. (c) Schematic illustration of lithium insertion into $CaFe_2O_4$ anode. (d) Cycling performance at a current density of 500 $mA{\cdot}g^{-1}$ up to 500 cycles[84] (Reprinted with permission, Copyright 2019, Elsevier). (e) TEM image of sintered $CaFe_2O_4$ nanofibers. (f) Crystal structure of $CaFe_2O_4$ nanofibers[85] (Reprinted with permission, Copyright 2020, IOPscience).

(Figs. 5(a)–5(c))[84]. The oxidants were metal salts, such as nitrate, sulfate, and carbonate. The reducing agents were urea, glycine, sucrose, starch, etc. The discharge capacity of porous $CaFe_2O_4$ was 561 $mA{\cdot}h{\cdot}g^{-1}$ after 150 cycles at a current density of 200 $mA{\cdot}g^{-1}$. In addition, the discharge capacity was about 437 $mA{\cdot}h{\cdot}g^{-1}$ after 500 cycles at a high current density of 500 $mA{\cdot}g^{-1}$ (Fig. 5(d)). In the synthesis process, the microporous were formed due to the release of many by-products (N_2, CO_2). The porous and chain-like skeleton structure effectively increased surface area, favoring the buffering volume change during the lithium insertion/de-insertion process and enlarging the contact between electrode and electrolyte. In the process of Li^+ insertion, $CaFe_2O_4$ was converted into Fe and CaO, and a new phase, Li_2O, was formed concurrently. The CaO acted as a buffer during cycling, preventing the aggregation of active nanoparticles and thus improving long-cycle stability. In addition, the mesoporous properties of $CaFe_2O_4$ allowed electrolytes to penetrate deeply into the anode, producing a high electrolyte saturation and redox activity. Meanwhile, the mesoporous structure also contributed to stress suppression. Furthermore, to explore the correlation between morphology, defect concentration, transport phenomena, and lithium storage performance, $CaFe_2O_4$ nanofibers (Fig. 5(e)) and nanoparticles were prepared by electrospinning and urea combustion methods, respectively[85]. The oxygen defects in $CaFe_2O_4$ nanofibers (Fig. 5(f)) facilitated the conductivity and the mobility of electrons/ions. In contrast to $CaFe_2O_4$ nanoparticles, the $CaFe_2O_4$ nanofibers exhibited impressive cycling and rate capability. The improved lithium storage performance of $CaFe_2O_4$ nanofibers was attributed to a high aspect ratio nanofiber network with void/gap structure. Also, a large number of oxygen defects facilitated faster electron/ion transfer, thus improving reaction kinetics.

In the meantime, reaction conditions, such as pH, annealing temperatures, and element ratios also play crucial roles. Spinel $SrFe_2O_4$ nanoparticles were prepared by a sol-gel method at different pH values[86]. Changing pH did not produce different phases and only changed the ion distribution in the lattice. Moreover, the XRD data showed that small changes in lattice were accompanied by changing cell size and density. It was due to the variations in ion distribution or oxygen supply. When preparing $SrFe_2O_4$ at different annealing temperatures, the ion distribution in the lattice changed with the increasing sintering temperature, eventually leading to a larger grain size[87].

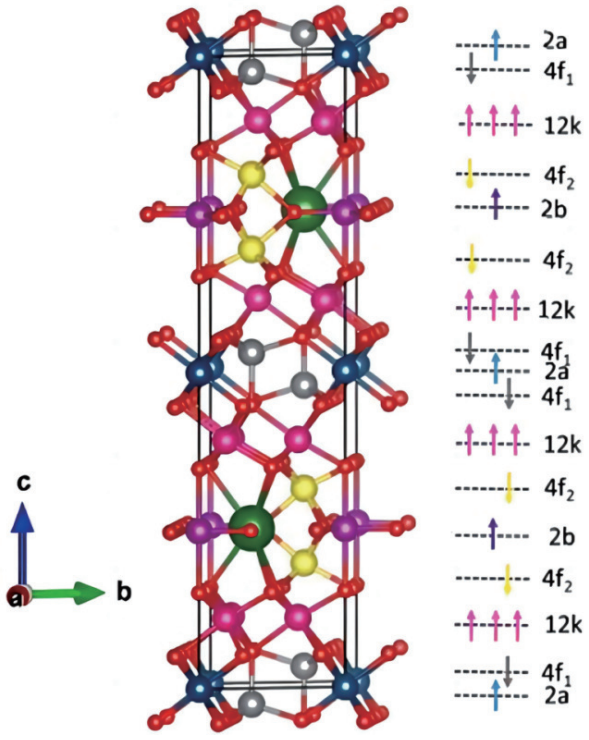

Fig. 6. (Color online) Unit cell diagram of $SrFe_{12}O_{19}$. Two large green spheres represent Sr atoms, while small red spheres represent O atoms. Fe atoms in each site are presented in different colors: 2a (blue), $4f_1$ (gray), 12k (pink), $4f_2$ (yellow), and 2b (purple)[91] (Reprinted with permission, Copyright 2021, Elsevier).

The cation radius in hexagonal magnetoplumbite ferrites is similar to the oxygen ion radius; therefore, the cations cannot enter gaps formed by oxygen ions and can only be in the same layer with oxygen ions[88]. Hexagonal magnetoplumbite ferrites can be divided into six types, namely M-type ($BaFe_{12}O_{19}$), Z-type ($Ba_3Me_2Fe_{24}O_{41}$), Y-type ($Ba_2Me_2Fe_{12}O_{22}$), W-type ($BaMe_2Fe_{16}O_{27}$), X-type ($Ba_2Me_2Fe_{28}O_{46}$), and U-type ($Ba_4Me_2Fe_{36}O_{60}$), where Me is Sr, Co, Ni, or Zn. Among them, the hexagonal magnetoplumbite ferrites with a general formula of $MeFe_{12}O_{19}$ (Me = Ba, Sr) have better physicochemical properties and can be used in various fields[89]. In the case of $SrFe_{12}O_{19}$ (Fig. 6)[90], the space group is P63/mmc. The cell structure has 64 atoms, containing 2 Sr atoms, 24 Fe atoms, and 38 O atoms. According to the difference in atomic equivalent occupancy, Fe atoms can be divided into five occupations: 2a, 2b, 4f1, 4f2, and 12k.

The properties of hexagonal magnetoplumbite ferrite $BaFe_{12}O_{19}$ are related to many factors. Under high-temperature annealing, preparing $BaFe_{12}O_{19}$ by a conventional solid-state method is inefficient, and it is easy to produce rough and uneven particles[92]. Also, the annealing temperature plays a decisive role in composition and morphology. $SrFe_{12}O_{19}$ nanoparticles were synthesized by a hydrothermal method[93]. As the annealing temperature increased, the content of $SrFe_{12}O_{19}$ and the intensity of the peaks in XRD spectra increased slightly (Fig. 7(a)), indicating that the microcrystals grew with the increased temperature. When the temperature reached 1200 °C, $SrFe_{12}O_{19}$ nanoparticles obviously aggregated, and the specific surface area decreased (Fig. 7(b)).

$BaFe_{12}O_{19}$ nanocrystals were prepared by a sol-gel method under a neutral condition, which delivered a reversible specific capacity of 959.5 mA·h·g^{-1} at 0.1 C and 358.3 mA·h·g^{-1} after 50 cycles (Figs. 7(c) and 7(d))[94]. $BaFe_{12}O_{19}$ was converted to Fe and Ba during the first discharge, and the nanocrystals decomposed utterly (Eq. (3)).

$$BaFe_{12}O_{19} + 38Li^+ + 38e^- \rightarrow 19Li_2O + 12Fe + Ba. \quad (3)$$

During charging, $BaFe_{12}O_{19}$ was no longer reversibly produced. Based on the reaction mechanism, the crystal structure was generally destroyed during the initial discharge. The Li_2O and the SEI layer caused an irreversible capacity loss in the first cycle. Fe and Ba showed a reversible electrochemical reaction to Li^+ in subsequent cycles (Eqs. (4) and (5)).

$$3Li_2O + 2Fe \leftrightarrow 6Li^+ + Fe_2O_3 + 6e^-, \quad (4)$$

$$Li_2O + Ba \leftrightarrow 2Li^+ + BaO + 2e^-. \quad (5)$$

Zn^{2+}-doped $BaFe_{12}O_{19}$ nanoplates were prepared by a hydrothermal method[95]. The reversible specific capacity was 665.5 mA·h·g^{-1} after 250 cycles at a current density of 100 mA·g^{-1} (Fig. 7(e)), which is much higher than that of pure $BaFe_{12}O_{19}$ nanoplates (441.5 mA·h·g^{-1}). Zn^{2+}-doped hexagonal $SrFe_{12}O_{19}$ nanoplates were prepared by the same synthesis strategy[96]. When the ratio of Fe/Sr was 6 : 1, the diffraction peaks of the product showed a good match with $SrFe_{12}O_{19}$, and there were no other phases (Fig. 7(f)). The reversible capacities of the Zn^{2+}-doped and undoped nanoplates were 1015.8 mA·h·g^{-1} and 456.5 mA·h·g^{-1} after 270 cycles at a current density of 100 mA·g^{-1}, respectively. The nanoplate structure relieved stress and strain during the repetitive lithium insertion/de-insertion process, maintaining structural integrity and improving cycling stability. Zn^{2+}-doped nanoplates had a smaller diameter, which provided more surface areas between the electrolyte and $SrFe_{12}O_{19}$, shortening the diffusion paths of Li^+ (Fig. 7(g)). Also, doping Zn^{2+} increased the lattice constant and promoted the migration of Li^+. Furthermore, the synergistic effect between elements was also an effective way to improve the conductivity and electrochemical cycling performance.

3. Alkaline earth metal brownmillerite oxides

According to the principle of crystallography, in perovskite oxides ABO_3 (A and B are cations), the A-site ions and oxygen ions together form an approximate cubic dense packing, the B-site ions and oxygen ions form BO_6 octahedra, the BO_6 octahedra are linked together with common vertices to create a network, and the A-site ions are located in the gaps of the network. The larger the radius of the A-site ions, the easier it is to form a perovskite structure. Conversely, a part of the BO_6 octahedra will be converted to BO_4 tetrahedra due to excessive oxygen loss during sintering. The structure of $ABO_{2.5}$ brownmillerite oxides is similar to perovskite oxides. It is obtained by replacing one-sixth of oxygen ions with vacancies, leading to the alternate arrangement of corner-shared BO_4 tetrahedra and BO_6 octahedra (Fig. 8)[97]. If a tetrahedron is specified to rotate vertically, the nearest corner-shared tetrahedron will turn in the opposite mode, producing different structure phases. Due to this unique construction, alkaline earth metal brownmillerite oxides have good properties in

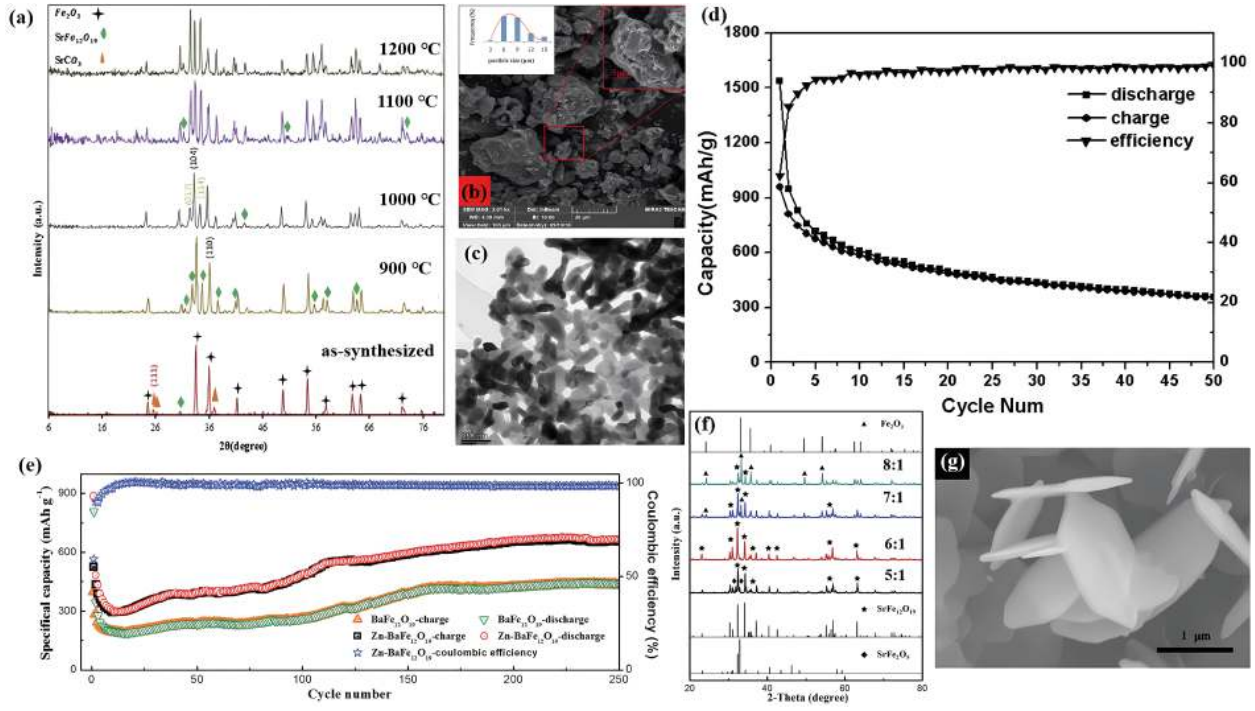

Fig. 7. (Color online) (a) XRD patterns of $SrFe_{12}O_{19}$ at different annealing temperatures. (b) FESEM image of $SrFe_{12}O_{19}$[93] (Reprinted with permission, Copyright 2018, Elsevier). (c) TEM images of the as-prepared $BaFe_{12}O_{19}$. (d) Cycle performance of $BaFe_{12}O_{19}$ electrode[94] (Reprinted with permission, Copyright 2013, Springer). (e) Cycling performance of $BaFe_{12}O_{19}$ and Zn^{2+}-doped $BaFe_{12}O_{19}$ nanoplates at a current density of 100 $mA{\cdot}g^{-1}$ and columbic efficiency of Zn^{2+}-doped $BaFe_{12}O_{19}$ nanoplates[95] (Reprinted with permission, Copyright 2015, The Royal Society of Chemistry). (f) XRD pattern of the powders synthesized by different Fe/Sr ratios. (g) SEM images of Zn^{2+}-doped $SrFe_{12}O_{19}$ nanoplates[96] (Reprinted with permission, Copyright 2017, The Royal Society of Chemistry).

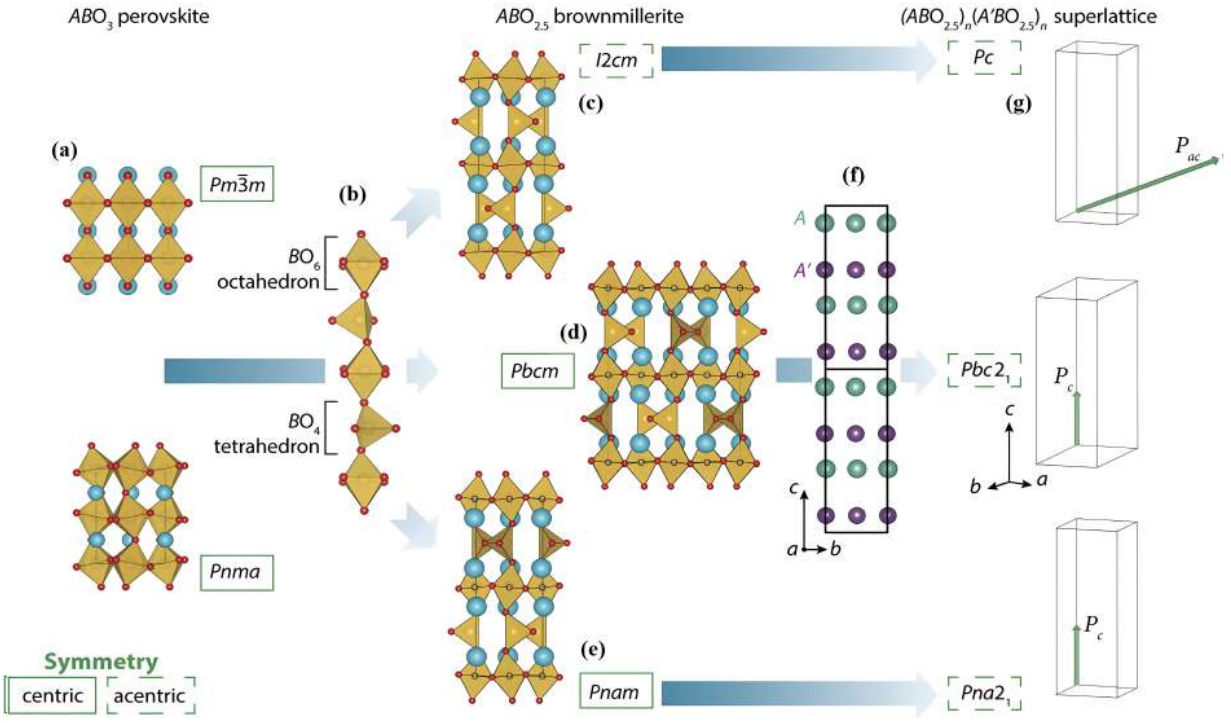

Fig. 8. (Color online) Design principles for realizing polar structures from nonpolar compounds through anion-vacancy and cation order. Starting from (a) fully oxidized perovskites are reduced in Step 1, resulting in (b) ordered rows of oxygen vacancies forming alternating layers of BO_6 octahedra and BO_4 tetrahedra. (c–e) Depict the resulting $ABO_{2.5}$ brownmillerites: the polar I2 cm and the nonpolar Pbcm and Pnam polymorphs that arise owing to the relative alignment of the BO_4 tetrahedra. Inversion centers are located at sites with octahedrally coordinated B cations, indicated by black open circles; not shown are the inversion centers situated on the unoccupied sites in the Pbcm and Pnam polymorphs. (f) In Step 2, chemically distinct A and A′ cations are ordered in layers along the ···BO6–BO4–BO6··· chain direction, which then removes all inversion centers and permits the net electric polarizations P indicated in (g)[97] (Reprinted with permission, Copyright 2017, The American Chemical Society).

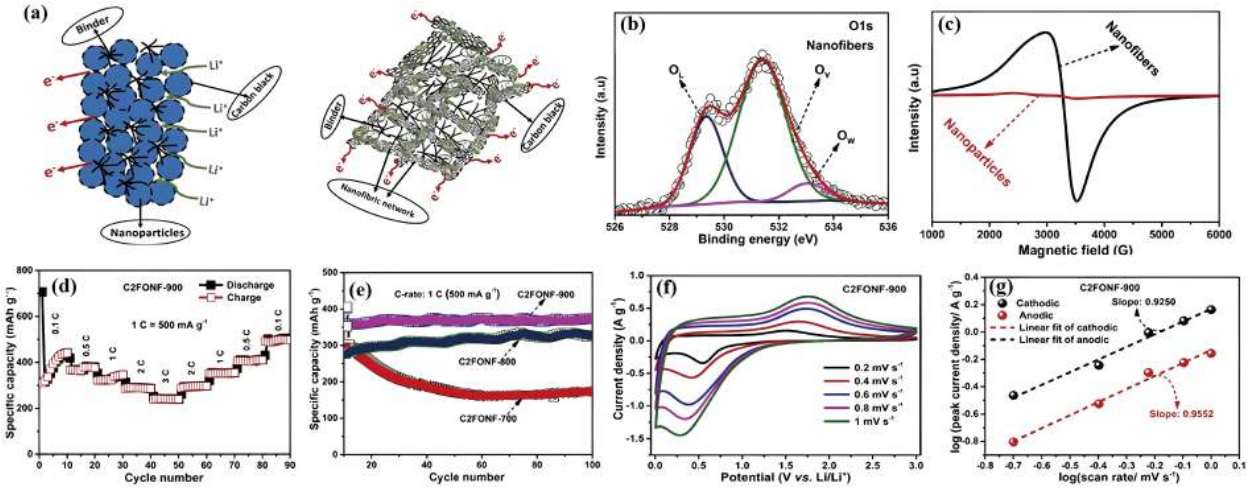

Fig. 9. (Color online) (a) Schematic illustration of lithium insertion/de-insertion in $Ca_2Fe_2O_5$ nanoparticles and nanofibers. (b) XPS and (c) EPR of nanofibers of $Ca_2Fe_2O_5$[98] (Reprinted with permission, Copyright 2020, The American Chemical Society). (d) Rate performance of C2FONF-900. (e) Comparative cyclic performance in $Ca_2Fe_2O_5$ electrodes in different annealing temperatures. (f) CV curves of C2FONF-900 at various scan rates. (g) log *i* vs. log *v* plot of C2FONF-900[103]. Copyright 2021, Elsevier.

Fig. 10. (Color online) Possible future development directions of alkaline earth metal iron-based oxide anodes.

electrochemical fields and have been highly studied in ion conduction and insertion.

$Ca_2Fe_2O_5$ nanoparticles and nanofibers were prepared, respectively[98]. Due to differences in microstructure and transmission properties, these two $Ca_2Fe_2O_5$ anodes also showed distinct lithium storage performance (Fig. 9(a)). Owing to the large size of $Ca_2Fe_2O_5$ nanoparticles, the buffering effect of CaO in the system was negligible. Unlike nanoparticles, nanofibers had a high and stable capacity because the nanofiber network contained voids/gaps that could accommodate stress/strain. Meanwhile, the large number of oxygen vacancies in nanofibers resulted in better conductivity, improving the lithium storage performance[99, 100]. X-ray photoelectron spectrometer (XPS) and electron paramagnetic resonance (EPR) confirmed that $Ca_2Fe_2O_5$ nanofibers had a high oxygen vacancy concentration (Figs. 9(b) and 9(c)). Typically, defects will cause atoms with lower coordination numbers to provide unsaturated coordination sites for oxygen chemical adsorption[101]. Notably, the EPR spectrum of the nanofibers showed a higher peak intensity which represented a higher oxygen vacancy concentration[102]. The oxygen vacancies ensured good electron/ion transport ability and enhanced reaction kinetics. In 2021, this group used a electrospinning method to prepare three kinds of $Ca_2Fe_2O_5$ nanofibers with different annealing temperatures and investigated their lithium storage performance[103]. The results showed that the influence of morphologies and oxygen vacancies on the electrochemical performance was generally coupled together. Despite $Ca_2Fe_2O_5$ nanofibers having larger particle sizes and lower surface areas, they still exhibited better rate performance by annealing at 900 °C (C2FONF-900) due to their higher oxygen defect concentration (Figs. 9(d) and 9(e)). The electrochemical behavior was mainly controlled by capacitance (Figs. 9(f) and 9(g)), and the higher capacitive Li^+ storage led to faster reaction kinetics at high sweep speed. Mesoporous $Ca_2Fe_2O_5$/α-Fe_2O_3 nanocomposites were synthesized by a solvothermal method combined with calcination processes[104]. The unique mesoporous nanostructure buffered volume changes and increased electrode/electrolyte contact areas, resulting in efficient Li^+ transmission and high capacitance-controlled specific capacity. Therefore, introducing a second phase or multiphase to prepare composite electrodes can produce a synergistic effect to realize phase-phase separation and resolve electrode damage.

4. Conclusions and perspectives

This review systematically introduces alkaline earth metal iron-based oxides for LIB anodes. It describes the synthesis methods, morphological characteristics, reaction mechanisms, and modifying strategies. Alkaline earth metal iron-

based oxides have the advantages of easy availability, low preparation cost, good thermal stability, stable chemical properties, and excellent electrochemical performance. Nonetheless, there are still some problems in this material system, such as low lithium storage capacity, unstable structure, and unclear electrochemical reaction mechanisms. By summarizing the current research progresses, some possible future research directions are put forward in the following (Fig. 10).

(1) Regulating crystallinity. The crystal structure of materials has a significant influence on Li^+ diffusion from surface to inside. The arrangement of atoms in crystals is periodic, whereas amorphous bodies have no long-range ordering. Theoretically, Li^+ inserted into crystal structures does not collide with original atoms and is more likely to be embedded and detached. In contrast, amorphous structures rapidly produce structural deformation, which is not conducive to lithium-ion diffusion. In most studies, the adjustment of crystallinity is usually caused by changing annealing temperatures, which generally varies the crystal structure, grain size, and lattice distance. Composites typically exhibit more amorphous because of the crystallization competition between phases. Proper amorphization can reduce rigidity, delivering better electrochemical performance. Therefore, crystallinity regulation may be a feasible way to improve the Li storage capability.

(2) Introducing defects and heteroatoms. Defect and doping engineering can increase electrochemical active sites, accelerate internal ion/electron transfer, and enhance conductivity. Defects are generally created by chemical reduction/etching or physical stripping/etching. Due to the exposure of active sites around defects, more lithium-ions can be anchored, favoring higher capacity. Defects can also modulate ion diffusion dynamic processes and increase intrinsic conductivity. In addition, oxygen vacancies in heterogeneous interfaces usually lead to uneven charge distribution and form a localized built-in electric field, facilitating ion diffusion/electron transport. Doping engineering improves lithium-ion diffusion by increasing lattice parameters. Besides, co-doping utilizes the synergistic effect of dopants to modulate electronic and chemical properties, accelerating the reaction of electrodes and lithium-ions for better electrochemical performance.

(3) Compositing with high conductive materials. Although alkaline earth metal iron-based oxides have many advantages as anodes, they still have poor conductivity and large volume change, leading to the pulverization of electrodes and the rapid decay of capacities. Alkaline-earth metal iron-based oxides composite with carbon can buffer volume expansion and prevent grain aggregation, facilitating better electrochemical performance. Also, carbon composites limit nanoparticle growth and shorten lithium-ion diffusion distance, providing good conductivity and stability. In addition to the above, alkaline earth metal iron-based oxides compounded with other metal oxides could integrate the advantages of components, realizing better reversible capacity and conductivity. The synergistic effect between phases inhibits volume expansion and provides stable cycling performance, showing great advantages and potential.

(4) Revealing electrochemical mechanisms. Exploring reaction mechanisms of alkaline earth iron-based oxides is of great importance because they generally undergo a complex conversion reaction. A precise mechanism can help researchers identify reaction processes and understand failure mechanisms, thus making reasonable improvement strategies. In recent years, characterization techniques such as *in situ* XRD, *in situ* TEM, and EXAFS have been able to reflect reaction mechanisms. Furthermore, the detailed observation of multiphase still needs to be explored. Therefore, there is an urgent need to utilize and develop advanced characterization techniques to investigate the mechanism more precisely.

All in all, despite many challenges, the exciting findings and excellent electrochemical properties make alkaline earth metal iron-based oxides promising lithium-ion electrodes. We believe that with further exploration and optimization of structural properties, alkaline earth metal oxides will exhibit better electrochemical performance. We hope our review will provide valuable information to promote the development of alkaline earth metal oxides as LIB anodes.

Acknowledgments

The authors acknowledge the support of the Shenyang University of Technology (QNPY202209-4), the National Natural Science Foundation of China (21571132), Jiangsu University Advanced Talent Fund (5501710002), and the Education Department of Liaoning Province (JYTQN2023285).

References

[1] Wu Y H, Xu R, Wang Z J, et al. Carbon-free crystal-like $Fe_{1-x}S$ as an anode for potassium-ion batteries. ACS Appl Mater Interfaces, 2021, 13, 55218

[2] Wu Y H, Xia W H, Liu Y Z, et al. Tungsten chalcogenides as anodes for potassium-ion batteries. Tungsten, 2023, 1

[3] Wu Y H, Zhao Z Q, Hao X R, et al. Cathode materials for calcium-ion batteries: Current status and prospects. Carbon Neutralization, 2023, 2, 551

[4] Luo Y X, Gao X Y, Dong M J, et al. Exploring the structural properties of cathode and anode materials in Li-ion battery via neutron diffraction technique. Chin J Struct Chem, 2023, 42, 100032

[5] Liang Y H, Wu W B, Li D P, et al. Highly stable lithium metal batteries by regulating the lithium nitrate chemistry with a modified eutectic electrolyte. Adv Energy Mater, 2022, 12, 2202493

[6] Wei Y R, Cheng J, Li D P, et al. A structure self-healing Li-rich cathode achieved by lithium supplement of Li-rich LLZO coating. Adv Funct Mater, 2023, 33, 2214775

[7] Zeng H H, Xing B L, Zhang C T, et al. In situ synthesis of MnO_2/porous graphitic carbon composites as high-capacity anode materials for lithium-ion batteries. Energy Fuels, 2020, 34, 2480

[8] Zhu L, Li F, Yao T H, et al. Electrospun $MnCo_2O_4$ nanotubes as high-performance anode materials for lithium-ion batteries. Energy Fuels, 2020, 34, 11574

[9] Hadouchi M, Koketsu T, Hu Z W, et al. The origin of fast-charging lithium iron phosphate for batteries. Battery Energy, 2022, 1, 20210010

[10] Shen S H, Zhang S Z, Deng S J, et al. Bioinspired large-scale production of multidimensional high-rate anodes for both liquid & solid-state lithium ion batteries. J Mater Chem A, 2019, 7, 22958

[11] Zeng J F, Yang L, Shao R W, et al. Mesoscopic $Ti_2Nb_{10}O_{29}$ cages comprised of nanorod units as high-rate lithium-ion battery anode. J Colloid Interface Sci, 2021, 600, 111

[12] Poizot P, Laruelle S, Grugeon S, et al. Nano-sized transition-metal oxides as negative-electrode materials for lithium-ion batteries. Nature, 2000, 407, 496

[13] Hong M, Su Y J, Zhou C, et al. Scalable synthesis of γ-Fe_2O_3/CNT composite as high-performance anode material for lithium-ion batteries. J Alloy Compd, 2019, 770, 116

[14] Wang J T, Ma C, Tang J W, et al. Facile fabrication of Fe_2O_3-decorated carbon matrixes with a multidimensional structure as anodes for lithium-ion batteries. Energy Fuels, 2021, 35, 816

[15] Wang Z Y, Li W L, Pan C F, et al. Carbon coated tetrakaidecahedron tin ferrite ($SnFe_2O_4$) with high pseudocapacitance as anode material for lithium-ion batteries. Appl Surf Sci, 2022, 587, 152870

[16] Gu H Y, Zhang Y M, Huang M Q, et al. Hydrolysis-coupled redox reaction to 3D Cu/Fe_3O_4 nanorod array electrodes for high-performance lithium-ion batteries. Inorg Chem, 2017, 56, 7657

[17] Mao J Y, Niu D C, Zheng N, et al. Fe_3O_4-embedded and N-doped hierarchically porous carbon nanospheres as high-performance lithium ion battery anodes. ACS Sustainable Chem Eng, 2019, 7, 3424

[18] Ma J A, Kong Y E, Liu S C, et al. Flexible phosphorus-doped graphene/metal–organic framework-derived porous Fe_2O_3 anode for lithium-ion battery. ACS Appl Energy Mater, 2020, 3, 11900

[19] Chen X F, Zhu X Y, Cao G P, et al. Fe_3O_4-based anodes with high conductivity and fast ion diffusivity designed for high-energy lithium-ion batteries. Energy Fuels, 2021, 35, 1810

[20] Musa N, Woo H J, Teo L P, et al. Optimization of Li_2SnO_3 synthesis for anode material application in Li-ion batteries. Mater Today:Proc, 2017, 4, 5169

[21] Deng S J, Zhu H, Wang G Z, et al. Boosting fast energy storage by synergistic engineering of carbon and deficiency. Nat Commun, 2020, 11, 132

[22] Shen S H, Guo W H, Xie D, et al. A synergistic vertical graphene skeleton and S-C shell to construct high-performance $TiNb_2O_7$-based core/shell arrays. J Mater Chem A, 2018, 6, 20195

[23] Yao Z J, Xia X H, Zhang Y, et al. Superior high-rate lithium-ion storage on $Ti_2Nb_{10}O_{29}$ arrays via synergistic TiC/C skeleton and N-doped carbon shell. Nano Energy, 2018, 54, 304

[24] Wu J B, Pan G X, Zhong W W, et al. Rational synthesis of $Cr_{0.5}Nb_{24.5}O_{62}$ microspheres as high-rate electrodes for lithium ion batteries. J Colloid Interface Sci, 2020, 562, 511

[25] Li Y Z, Meng Y S, Liu X L, et al. Double-protected zinc ferrite nanospheres as high rate and stable anode materials for lithium ion batteries. J Power Sources, 2019, 442, 227256

[26] Luo L, Chen Z, Ke H Z, et al. Facile synthesis of three-dimensional $MgFe_2O_4$/graphene aerogel composites for high lithium storage performance and its application in full cell. Mater Des, 2019, 182, 108043

[27] Bhujun B, Tan M T T, Shanmugam A S. Study of mixed ternary transition metal ferrites as potential electrodes for supercapacitor applications. Results Phys, 2017, 7, 345

[28] Datt G, Kotabage C, Abhyankar A C. Ferromagnetic resonance of $NiCoFe_2O_4$ nanoparticles and microwave absorption properties of flexible $NiCoFe_2O_4$-carbon black/poly(vinyl alcohol) composites. Phys Chem Chem Phys, 2017, 19, 20699

[29] Zeng Z X, Lan M S, Zhang Q, et al. Effect of solution concentration on magnetoelectric properties of barium ferrite ceramics. Appl Phys A, 2021, 127, 946

[30] Bock D C, Tallman K R, Guo H Y, et al. (De)lithiation of spinel ferrites Fe_3O_4, $MgFe_2O_4$, and $ZnFe_2O_4$: A combined spectroscopic, diffraction and theory study. Phys Chem Chem Phys, 2020, 22, 26200

[31] Ortiz-Quiñonez J L, Das S, Pal U. Catalytic and pseudocapacitive energy storage performance of metal (Co, Ni, Cu and Mn) ferrite nanostructures and nanocomposites. Prog Mater Sci, 2022, 130, 100995

[32] Li J B, Li Z H, Ning F Y, et al. Ultrathin mesoporous Co_3O_4 nanosheet arrays for high-performance lithium-ion batteries. ACS Omega, 2018, 3, 1675

[33] Feng D Y, Yang H, Guo X Z. 3-Dimensional hierarchically porous $ZnFe_2O_4$/C composites with stable performance as anode materials for Li-ion batteries. Chem Eng J, 2019, 355, 687

[34] Ma J Y, Guo E Y, Yin L W. Porous hierarchical spinel Mn-doped $NiCo_2O_4$ nanosheet architectures as high-performance anodes for lithium-ion batteries and electrochemical reaction mechanism. J Mater Sci, 2019, 30, 8555

[35] Liu Q, Hu Y H, Yu X R, et al. The pursuit of commercial silicon-based microparticle anodes for advanced lithium-ion batteries: A review. Nano Res Energy, 2022, 1, e9120037

[36] Sivakumar N, Gnanakan S R P, Karthikeyan K, et al. Nanostructured $MgFe_2O_4$ as anode materials for lithium-ion batteries. J Alloys Compd, 2011, 509, 7038

[37] Rezaie E, Rezanezhad A, Hajalilou A, et al. Electrochemical behavior of $SrFe_{12}O_{19}$/$CoFe_2O_4$ composite nanoparticles synthesized via one-pot hydrothermal method. J Alloys Compd, 2019, 789, 40

[38] Araújo J C R, Araujo-Barbosa S, Souza A L R, et al. Tuning structural, magnetic, electrical, and dielectric properties of $MgFe_2O_4$ synthesized by sol-gel followed by heat treatment. J Phys Chem Solids, 2021, 154, 110051

[39] de Hoyos-Sifuentes D H, Reséndiz-Hernández P J, Díaz-Guillén J A, et al. Synthesis and characterization of $MgFe_2O_4$ nanoparticles and PEG-coated $MgFe_2O_4$ nanocomposite. J Mater Res Technol, 2022, 18, 3130

[40] Adewuyi A, Gervasi C A, Mirífico M V. Synthesis of strontium ferrite and its role in the removal of methyl orange, phenolphthalein and bromothymol blue from laboratory wastewater. Surf Interfaces, 2021, 27, 101567

[41] Naaz F, Dubey H K, Kumari C, et al. Structural and magnetic properties of $MgFe_2O_4$ nanopowder synthesized via co-precipitation route. SN Appl Sci, 2020, 2, 808

[42] Ghahfarokhi S E M, Shobegar E M, Shoushtari M Z. Preparation and characterization of spinel $SrFe_2O_4$ nanoparticles by method sol-gel. J Aust Ceram Soc, 2021, 57, 1359

[43] Yamaguchi A, Sako H, Miyauchi M. Synthesis of $CaFe_2O_4$ nanorod thin film using molten salt method and analysis of its photoelectrochemical properties. Chem Lett, 2020, 49, 1462

[44] Guo L, Okinaka N, Zhang L, et al. Molten salt-assisted shape modification of $CaFe_2O_4$ nanorods for highly efficient photocatalytic degradation of methylene blue. Opt Mater, 2021, 119, 111295

[45] Guo Y, Qin G H, Liang E Q, et al. MOFs-derived $MgFe_2O_4$ microboxes as anode material for lithium-ion batteries with superior performance. Ceram Int, 2017, 43, 12519

[46] Wang H, Yang Q, Zheng N, et al. Roadmap of amorphous metal-organic framework for electrochemical energy conversion and storage. Nano Res, 2023, 16, 4107

[47] Permien S, Indris S, Scheuermann M, et al. Is there a universal reaction mechanism of Li insertion into oxidic spinels: A case study using $MgFe_2O_4$. J Mater Chem A, 2015, 3, 1549

[48] Guo H Y, Durham J L, Brady A B, et al. Essential role of spinel $MgFe_2O_4$ surfaces during discharge. J Electrochem Soc, 2020, 167, 090506

[49] Tan Q K, Wang C, Cao Y D, et al. Synthesis of a zinc ferrite effectively encapsulated by reduced graphene oxide composite anode material for high-rate lithium ion storage. J Colloid Interface Sci, 2020, 579, 723

[50] Zhang M Y, Liu Y, Zhu H T, et al. Hierarchical bead chain $ZnFe_2O_4$-PEDOT composites with enhanced Li-ion storage properties as anode materials for lithium-ion batteries. Appl Surf Sci, 2020, 529, 147078

[51] Wu Y H, Wu X N, Guan Y Y, et al. Carbon-based flexible elec-

trodes for electrochemical potassium storage devices. New Carbon Mater, 2022, 37, 852
[52] Zhu H F, Sha M, Zhao H P, et al. Highly-rough surface carbon nanofibers film as an effective interlayer for lithium–sulfur batteries. J Semicond, 2020, 41, 092701
[53] Wu Y H, Chen G B, Wu X N, et al. Research progress on vanadium oxides for potassium-ion batteries. J Semicond, 2023, 44, 041701
[54] He S J, Wang Z D, Wang Z J, et al. Recent progress and future prospect of novel multi-ion storage devices. J Semicond, 2023, 44, 040201
[55] Wang X H, Wang H L. Designing carbon anodes for advanced potassium-ion batteries: Materials, modifications, and mechanisms. Adv Powder Mater, 2022, 1, 100057
[56] Ding C Y, Wang L J, Zhou W W, et al. New design on Li-ion battery anode of ternary complex metal/metal oxide@CNT: A case study of hierarchical NiCo-$NiCo_2O_4$@CNTs. Chem Eng J, 2018, 353, 340
[57] Han W J, Qin X Y, Wu J X, et al. Electrosprayed porous Fe_3O_4/carbon microspheres as anode materials for high-performance lithium-ion batteries. Nano Res, 2018, 11, 892
[58] Zhang Y T, Zhang Y L, Zhang K B, et al. Nitrogen-doped graphene nanosheet coated nanospherical Fe_3O_4 from zeolitic imidazolate frameworks template as anode of lithium ion batteries. Energy Fuels, 2020, 34, 14986
[59] Zhao C H, Fan J T, Guo J J, et al. Dual carbon-supported ZnO/CuO nanocomposites as an anode with improved performance for Li-ion batteries. Energy Fuels, 2022, 36, 5483
[60] Tang Y K, Wang H R, Zhang Y, et al. *In-situ* reduction synthesis of one dimensional hybrid porous TiO@C anode for high-performance Li-ion storage. Ceram Int, 2021, 47, 5832
[61] Yin Y H, Liu W F, Huo N N, et al. Synthesis of vesicle-like $MgFe_2O_4$/graphene 3D network anode material with enhanced lithium storage performance. ACS Sustainable Chem Eng, 2017, 5, 563
[62] Yu Y, Li M T, Li Q W, et al. Core-shell $MgFe_2O_4$@C nano-composites derived via thermal decomposition-reduction dual strategy for superior lithium storage. J Alloys Compd, 2020, 834, 155207
[63] Wang B, Ruan T T, Chen Y, et al. Graphene-based composites for electrochemical energy storage. Energy Storage Mater, 2020, 24, 22
[64] Liu W F, Gao R Z, Zhang H S, et al. Improving the cycle performance of $MgFe_2O_4$ anode material based on the spatial limiting effect. J Alloys Compd, 2021, 865, 158668
[65] Liu W F, Gao R Z, Yin Y H, et al. 3D hierarchical porous N-doped carbon nanosheets/$MgFe_2O_4$ composite as anode material with excellent cycling stability and rate performance. Scr Mater, 2020, 189, 36
[66] Gan Q M, Zhao K M, He Z, et al. Zeolitic imidazolate framework-8-derived N-doped porous carbon coated olive-shaped FeO_x nanoparticles for lithium storage. J Power Sources, 2018, 384, 187
[67] Peng M X, Qiu Y C, Zhang M X, et al. Improved electrochemical performance of SiO-based anode by N, P binary doped carbon coating. Appl Surf Sci, 2020, 507, 145060
[68] Ma C R, Deng C J, Liao X Z, et al. Nitrogen and phosphorus codoped porous carbon framework as anode material for high rate lithium-ion batteries. ACS Appl Mater Interfaces, 2018, 10, 36969
[69] Guo L Z, He H Y, Ren Y R, et al. Core-shell SiO@F-doped C composites with interspaces and voids as anodes for high-performance lithium-ion batteries. Chem Eng J, 2018, 335, 32
[70] Liu Y, Yang H H, Zheng H Y, et al. Structural characteristics and electrochemical performance of N, P-codoped porous carbon as a lithium-ion battery anode electrode. ACS Omega, 2022, 7, 34109
[71] Sun Y Q, Fu W, Hu Y X, et al. The role of tungsten-related elements for improving the electrochemical performances of cathode materials in lithium ion batteries. Tungsten, 2021, 3, 245
[72] Liu W F, Pang Y D, Shi Z P, et al. Ultrafast kinetics in a PAN/$MgFe_2O_4$ flexible free-standing anode induced by heterojunction and oxygen vacancies. ACS Appl Mater Interfaces, 2022, 14, 11575
[73] Yin X X, Shao X, Liang S J, et al. Preparation of well-dispersed $MgFe_2O_4$ nanospheres and their electrochemical performance for lithium-ion batteries. Bull Mater Sci, 2021, 44, 21
[74] Yin Y H, Huo N N, Liu W F, et al. Hollow spheres of $MgFe_2O_4$ as anode material for lithium-ion batteries. Scr Mater, 2016, 110, 92
[75] Han C H, Zhang X, Xu X M, et al. Porous $CaFe_2O_4$ as a promising lithium ion battery anode: A trade-off between high capacity and long-term stability. Nanoscale, 2018, 10, 12963
[76] Gong C, Bai Y J, Qi Y X, et al. Preparation of carbon-coated $MgFe_2O_4$ with excellent cycling and rate performance. Electrochim Acta, 2013, 90, 119
[77] Luo L, Li D W, Zang J, et al. Carbon - coated magnesium ferrite nanofibers for lithium - ion battery anodes with enhanced cycling performance. Energy Technol, 2017, 5, 1364
[78] Yin Y H, Liu W F, Huo N N, et al. High rate capability and long cycle stability of Fe_2O_3/$MgFe_2O_4$ anode material synthesized by gel-cast processing. Chem Eng J, 2017, 307, 999
[79] Lee S B, Balasubramaniam R. Double-shelled hybrid $MgFe_2O_4$/Fe_2O_3 hollow microspheres as a high-capacity anode for lithium-ion batteries. J Ind Eng Chem, 2022, 110, 262
[80] Yin Y H, Liu W F, Gao R Z, et al. A 3D porous $MgFe_2O_4$ integrative electrode as a binder-free anode with high rate capability and long cycle lifetime. ChemElectroChem, 2019, 6, 757
[81] Wang D, Wu J L, Bai D X, et al. Mesoporous spinel ferrite composite derived from a ternary MgZnFe-layered double hydroxide precursor for lithium storage. J Alloys Compd, 2017, 726, 306
[82] Xu C X, Manukyan K V, Adams R A, et al. One-step solution combustion synthesis of CuO/Cu_2O/C anode for long cycle life Li-ion batteries. Carbon, 2019, 142, 51
[83] Adams R A, Pol V G, Varma A. Tailored solution combustion synthesis of high performance $ZnCo_2O_4$ anode materials for lithium-ion batteries. Ind Eng Chem Res, 2017, 56, 7173
[84] Shaji N, Santhoshkumar P, Nanthagopal M, et al. Electrochemical performance of porous $CaFe_2O_4$ as a promising anode material for lithium-ion batteries. Appl Surf Sci, 2019, 491, 757
[85] Sundriyal S K, Sharma Y. Revealing the effect of oxygen defects and morphology on Li-storage performance of calcium iron oxide. J Electrochem Soc, 2020, 167, 110526
[86] Mousavi Ghahfarokhi S E, Shobegar E M. Influence of pH on the structural, magnetic and optical properties of $SrFe_2O_4$ nanoparticles. J Mater Res Technol, 2020, 9, 12177
[87] Mousavi Ghahfarokhi S E, Shobegar E M, Shoushtari M Z. Effects of sintering temperature on structural, morphological and magnetic properties of strontium ferrite nanoparticles. J Supercond Nov Magn, 2019, 32, 1067
[88] Zhu S M, Fu J C, Li H L, et al. Direct observation of magnetocrystalline anisotropy tuning magnetization configurations in uniaxial magnetic nanomaterials. ACS Nano, 2018, 12, 3442
[89] Marouani Y, Massoudi J, Noumi M, et al. Electrical conductivity and dielectric properties of Sr doped M-type Barium hexaferrite $BaFe_{12}O_{19}$. RSC Adv, 2021, 11, 1531
[90] Wang Z, Zha X H, Wu Z, et al. First-principles study on electronic and magnetic properties of Mn-doped strontium ferrite $SrFe_{12}O_{19}$. J Inorg Mater, 2019, 34, 1047
[91] Lamouri R, Daoudi K, Absike H, et al. Structural, electronic and magnetic properties of Co-substituted $SrFe_{12}O_{19}$: A DFT study. Mater Today Commun, 2021, 28, 102589

[92] Topal U, Ozkan H, Dorosinskii L. Finding optimal Fe/Ba ratio to obtain single phase $BaFe_{12}O_{19}$ prepared by ammonium nitrate melt technique. J Alloys Compd, 2007, 428, 17
[93] Rezaie E, Rezanezhad A, Ghadimi L S, et al. Effect of calcination on structural and supercapacitance properties of hydrothermally synthesized plate-like $SrFe_{12}O_{19}$ hexaferrite nanoparticles. Ceram Int, 2018, 44, 20285
[94] Zhao Y, Huang Y, Wang Q F, et al. Preparation of $BaFe_{12}O_{19}$ as anode material for lithium-ion batteries through sol-gel method. J Sol-Gel Sci Technol, 2013, 66, 238
[95] Hu C X, Qiu S, Lu G X, et al. Enhanced electrochemical performance of Barium hexaferrite nanoplates by Zn^{2+} doping serving as anode materials. RSC Adv, 2015, 5, 70749
[96] Hu C X, Cao H L, Wang S Y, et al. Synthesis of strontium hexaferrite nanoplates and the enhancement of their electrochemical performance by Zn^{2+} doping for high-rate and long-life lithium-ion batteries. New J Chem, 2017, 41, 6427
[97] Young J, Moon E J, Mukherjee D, et al. Polar oxides without inversion symmetry through vacancy and chemical order. J Am Chem Soc, 2017, 139, 2833
[98] Sundriyal S K, Sharma Y. Role of oxygen deficiency and microstructural voids/gaps in nanostructures of $Ca_2Fe_2O_5$ as an anode toward next-generation high-performance Li-ion batteries. ACS Appl Energy Mater, 2020, 3, 6360
[99] Wang W X, Xiong F Y, Zhu S H, et al. Defect engineering in molybdenum-based electrode materials for energy storage. eScience, 2022, 2, 278
[100] Yang L, Zeng J F, Zhou L, et al. Orderly defective superstructure for enhanced pseudocapacitive storage in titanium niobium oxide. Nano Res, 2022, 15, 1570
[101] Zhang S M, Wang X H, Li Y, et al. Moderate oxygen-deficient Fe(III) oxide nanoplates for high performance symmetric supercapacitors. J Colloid Interface Sci, 2020, 565, 458
[102] Zhang Y P, Zhang M Q, Liu Y Y, et al. Oxygen vacancy regulated $TiNb_2O_7$ compound with enhanced electrochemical performance used as anode material in Li-ion batteries. Electrochim Acta, 2020, 330, 135299
[103] Sundriyal S K, Sharma Y. Controlled generation and tuning the oxygen defects in nanofibers of $Ca_2Fe_2O_5$ toward high and stable Li-ion battery anode. Appl Surf Sci, 2021, 560, 150055
[104] Zhang K, Liang S J, Yin X X, et al. Mesoporous $Ca_2Fe_2O_5/\alpha$-Fe_2O_3 nanocomposite anode for lithium-ion batteries. J Solid State Chem, 2020, 286, 121300

Mingyuan Ye is currently a graduate student at Shenyang University of Technology. Her research interest is nanostructural metal oxide-based anode materials for lithium-ion batteries.

Xiaorui Hao is currently a graduate student at Nanjing Tech University. Her research focuses on zinc-ion battery electrolytes and the interphase chemistry of electrodes/electrolytes.

Lin Li is an Oujiang Distinguished Professor and associate dean of the Institute for Carbon Neutralization, College of Chemistry and Materials Engineering, Wenzhou University. He received his B.S. degree in materials science and engineering from Nanchang University (2016). He obtained his Ph.D. from Nankai University in 2021. His research focuses on advanced electrode materials and electrolytes for lithium-ion batteries, sodium-ion batteries, and potassium-ion batteries.

Chenglin Zhang is currently a Jinshan Youth Distinguished Professor at Jiangsu University, China. He received his Ph.D. degree in Applied Physics from Institute of Physics, Technische Universität Ilmenau in 2022. His research mainly focuses on new electrochemical energy storage devices, such as sodium- and potassium-ion batteries, and hybrid ion capacitors.

Fanian Shi received his Ph.D. in applied chemistry in 1996 at Changchun Institute of Applied Chemistry, Chinese Academy of Sciences. He is currently a full professor at the Shenyang University of Technology and a member of the committee on Energy and Environment, China Energy Society. He specializes in the research of MOF composites for energy materials, photocatalysts, etc.

Yuhan Wu received his Ph.D. degree in material physics at the Ilmenau University of Technology in 2021. Since 2022, he has been an associate professor at the Shenyang University of Technology. His research interests focus on designing and synthesizing multi-scale materials for energy conversion and storage.